Experimental Verification of Models for Microfabricated Piezoelectric Vibration Energy Harvesters

Noel E. duToit[*] and Brian L. Wardle[†]

Massachusetts Institute of Technology, Cambridge, Massachusetts 02139

Experiments have been performed to verify power-optimized modal models of piezoelectric vibration harvesters for microelectromechanical systems. Such harvesters can power a variety of sensors, and there have been recent national workshops dedicated to harvesting. Detailed experimental results, including displacement histories and electrical output, are provided over a range of frequencies and electrical loadings to compare with (optimized) modal models. The harvester geometry considered is that of a symmetric bimorph macroscale cantilever. Although some experimental work for cantilevered bimorph harvesters has been published, key testing and/or device parameters needed for model verification are missing and/or data at and near power optima (the most interesting operating points) are not provided. Therefore, a detailed set of experiments was performed using power-optimized modeling results to guide the test matrix. Over the broad range of parameters tested, the models accurately predicted all trends and device performance away from device resonances (resonance and antiresonance frequencies). Near the resonance frequencies, the model consistently underpredicts electrical performance, which is satisfactorily attributed (and experimentally supported) to the well-known piezoelectric coupling nonlinearity in the large-strain region. The data presented herein can serve as benchmark data to verify other modeling efforts. The verified models have been used to optimally design microelectromechanical system harvesters for commercial aircraft and microfabrication is ongoing.

Nomenclature

$\boldsymbol{B}_f$	=	modal forcing vector with elements $B_{f,k}$, kg
b	=	width of structure, m
$\boldsymbol{C}$	=	damping matrix with elements C_{kl}, N $\cdot$ s/m
$\boldsymbol{C}_p$	=	capacitive coefficient matrix with elements $C_{p,kl}$, F
$\boldsymbol{c}$	=	elastic stiffness matrix with elements c_{kl}, Pa
$\boldsymbol{e}$	=	piezoelectric constant matrix with elements e_{kl}, C/m^2
e_n	=	electrode numbering
f	=	frequency, Hz
i	=	current, A
$\boldsymbol{K}$	=	modal stiffness matrix with elements K_{kl}, N/m
L	=	device length, m
$\boldsymbol{M}$	=	modal mass matrix with elements M_{kl}, kg
m	=	mass per length, kg/m
P_{out}	=	power developed/extracted, W
$\boldsymbol{q}$	=	charge vector with scalar value q_j, C
R_l	=	electrical resistance, Ω
$\boldsymbol{r}$	=	generalized relative displacement vector with elements r_i, m
t	=	thickness of device layer, m
V	=	volume, m^3
$\boldsymbol{v}$	=	voltage vector with elements v_j, V
w	=	absolute displacement, m
w_B	=	absolute base displacement, m
x	=	Cartesian coordinate, m
α	=	dimensionless time constant
$\boldsymbol{\varepsilon}$	=	permittivity matrix with elements ε_{kl}, F/m
ζ_m	=	mechanical damping ratio
$\boldsymbol{\Theta}$	=	coupling coefficient matrix with elements θ_{kl}, N/V
κ	=	electromechanical system coupling coefficient
ρ	=	density of device layer, kg/m^3
$\boldsymbol{\psi}_r$	=	mechanical mode shape vector of elements $\psi_{r,i}$
$\boldsymbol{\psi}_v$	=	electrical mode shape vector of elements $\psi_{v,j}$
Ω	=	frequency ratio
ω	=	frequency, rad/s
∇	=	gradient operator

Subscripts

a	=	axial direction
ar	=	variable evaluated at antiresonance frequency
e	=	effective parameter
i	=	mechanical mode numbering
j	=	electrical mode numbering
k	=	matrix row index or vector index
l	=	matrix column index
mp	=	variable evaluated between resonances
n	=	electrode element numbering or piezoelectric element numbering in the bimorph
opt	=	power-optimized variable
p	=	piezoelectric layer property
r	=	variable evaluated at resonance frequency
s	=	structural (nonpiezoelectric) layer property
t	=	thickness direction
tip	=	variable evaluated at tip of device

Superscripts

E	=	variable at constant electric field
l	=	material (piezoelectric) local coordinates
S	=	variable at constant strain
t	=	vector or matrix transpose
$*$	=	beam effective properties

*Currently Graduate Student at California Institute of Technology, Department of Mechanical Engineering, 1200 East California Boulevard, Pasadena, CA 91125; ndutoit@caltech.edu. AIAA Student Member (Corresponding Author).

†Boeing Assistant Professor, Technology Laboratory for Advanced Materials and Structures, Department of Aeronautics and Astronautics; wardle@mit.edu. Member AIAA.

I. Introduction

$\mathbf{S}$ YSTEMS of ubiquitous, low-cost, self-organizing agents, or nodes (distributed wireless microsensor networks) have been the research focus of multiple groups in recent years [1]. These networks find application in many areas including building climate control, warehouse inventory and supply chain control, identification and personalization (RFID tags), the smart home [2], and structural health monitoring (SHM). A major concern for these networks is the power supply to each node [3]. The power requirement for these node networks has been driven down and power consumption of tens to hundreds of μW per node is predicted [2,4–6]. As a result, self-powered nodes have become feasible and can be realized through the conversion of ambient energy to usable electrical energy. Ambient power sources (e.g., thermal gradients, vibration, fluid flow, solar, etc.) have been investigated for long-term implementation of sensor node networks and the research is reviewed by duToit et al. [7]. Harvesting mechanical vibrations is a viable source of power, well matched to the needs of wireless sensor nodes, and is the focus of the current research (mechanical vibrations occur pervasively in the environment). This work focuses on cantilevered resonant devices vs the also common patch-type of harvester (refer to Moheimani [8] for a survey of recent developments in vibration damping using piezoelectric transducers). Specifically, a microelectromechanical systems (MEMS) mechanical vibration energy harvester is desirable for its small size, low cost, and on-chip integration with state-of-the-art sensors.

An optimized, fully electromechanically coupled model has been presented (refer to duToit et al. [7,9]). Although some experimental work for cantilevered bimorph harvesters has been published [3,10], key testing and/or device parameters needed for model verification are missing and/or data at and near power optima (the most interesting operating points) are not provided. Thus, the open literature lacks sufficient experimental data for model verification. This report focuses on experimental data obtained for a macroscale cantilevered bimorph piezoelectric energy harvester. A detailed implementation of the model (presented elsewhere) has been included for the geometry of the test device. The implemented model is verified by comparison to mechanical and electrical experimental data so that it can be applied to device design or analysis problems. The design of a MEMS-scale piezoelectric energy harvester has been presented [9,11], developed with a concurrent microfabrication process, using the verified models.

II. Modeling of Piezoelectric Vibration Energy Harvester

A coupled electromechanical model for a cantilevered piezoelectric structure has been presented [7,9,11], including the optimization of the governing equations for maximum power extraction at the resonances. The model is based on a modal analysis, combined with the small-signal piezoelectric material constitutive law. Each harvester has the following components: the cantilevered beam structure, piezoelectric element(s), and electrodes. A proof mass is included as it can be added to drive the natural frequency down (as would be desired to harvest maximum available ambient energy, for example, aircraft have maximum available energy in the range of 0.1–1 kHz [12,13]). Two piezoelectric modes of operation are possible for this configuration: the {3-1} mode and the {3-3} mode. For the {3-1} mode, the strain is applied perpendicular to the poling direction, whereas the strain is applied along the poling axis for the {3-3} mode of operation. This analysis focuses on the {3-1} mode of operation of a bimorph cantilever harvester because the experimental device is operated in this mode.

For the piezoelectric bimorph harvester configuration, the active elements can be connected in one of two ways (depending on the poling of the elements): when the two piezoelectric elements are poled in the same global direction, the device is connected in parallel. When the two active elements are poled in opposite directions, the device is connected in series. Both wiring options result in the same power, but the series connection develops double the voltage and half the current as compared to the parallel connection. This paper focuses on this configuration for model implementation. The model and optimization presented previously [7,9,11] is outlined in the next section, before the model is adapted for the experimental bimorph harvester connected in series.

A. Governing Equations and Optimization

In prior work, a coupled electromechanical model for a base-excited cantilever beam with a mass at the free end is presented [7,9,11]. The model can be obtained with an energy method approach. The model is based on a modal decomposition of the mechanical response of the system combined with the small-signal linear constitutive law for piezoelectric materials. The model is fairly general and has been implemented for {3-1}-mode bimorph configurations (as herein) and {3-1}- and {3-3}-mode unimorph configurations. A detailed analysis of the relationship between poling direction, piezoelectric constants, and applied and developed electric fields is included in [9]. The general multi-degree-of-freedom (DOF) governing equations are

$$\boldsymbol{M}\ddot{\boldsymbol{r}} + \boldsymbol{C}\dot{\boldsymbol{r}} + \boldsymbol{K}\boldsymbol{r} - \boldsymbol{\Theta}\boldsymbol{v} = -\boldsymbol{B}_f\ddot{w}_B \qquad (1)$$

$$\boldsymbol{\Theta}^{\,t}\boldsymbol{r} + \boldsymbol{C}_p\boldsymbol{v} + \boldsymbol{q} = 0 \qquad (2)$$

The overhead dot indicates a time derivative, $\boldsymbol{v}$ is the voltage developed, $\boldsymbol{q}$ is the charge, and $\boldsymbol{r}$ is the generalized relative displacement. $\boldsymbol{r}$ is a vector whose length is determined by the number of mechanical modes considered, whereas vectors $\boldsymbol{v}$ and $\boldsymbol{q}$ have length equal to the number of electrode pairs. $\ddot{w}_B$ is the absolute base input acceleration, that is, the source of mechanical energy being harvested. The mass ($\boldsymbol{M}$), stiffness ($\boldsymbol{K}$), coupling ($\boldsymbol{\Theta}$), capacitive matrices ($\boldsymbol{C}_p$), and forcing vector ($\boldsymbol{B}_f$) are obtained from a calculus of variations analysis:

$$\boldsymbol{M} = \int_{V_s} \boldsymbol{\psi}_r^t \rho_s \boldsymbol{\psi}_r \, \mathrm{d}V_s + \int_{V_p} \boldsymbol{\psi}_r^t \rho_p \boldsymbol{\psi}_r \, \mathrm{d}V_p \qquad (3)$$

$$\boldsymbol{K} = \int_{V_s} \left(-x_t\boldsymbol{\psi}_r''\right)^t \boldsymbol{c}_s \left(-x_t\boldsymbol{\psi}_r''\right) \mathrm{d}V_s + \int_{V_p} \left(-x_t\boldsymbol{\psi}_r''\right)^t \boldsymbol{c}^E \left(-x_t\boldsymbol{\psi}_r''\right) \mathrm{d}V_p \qquad (4)$$

$$\boldsymbol{\Theta} = \int_{V_p} \left(-x_t\boldsymbol{\psi}_r''\right)^t \boldsymbol{e}^t (-\nabla\boldsymbol{\psi}_v) \, \mathrm{d}V_p \qquad (5)$$

$$\boldsymbol{C}_p = \int_{V_p} (-\nabla\boldsymbol{\psi}_v)^t \boldsymbol{\varepsilon}^S (-\nabla\boldsymbol{\psi}_v) \, \mathrm{d}V_p \qquad (6)$$

$$\boldsymbol{B}_f = \int_0^L m(x_a)\boldsymbol{\psi}_r^t \, \mathrm{d}x_a = m\int_0^L \boldsymbol{\psi}_r^t \, \mathrm{d}x_a \qquad (7)$$

$\boldsymbol{\psi}_r$ is the mechanical modes, $\boldsymbol{\psi}_v$ is the electrical modes (one for each electrode pair), $\boldsymbol{\varepsilon}^S$ is the permittivity at constant stress, $\boldsymbol{e}$ is the piezoelectric coupling constant, and the prime indicates a spatial derivative. $\boldsymbol{c}^E$ is the elastic stiffness of the piezoelectric material at constant electric field, and $\boldsymbol{c}_s$ is the elastic stiffness of the structure. ρ is the density and V is the volume (subscripts p and s indicate a property of the piezoelectric and structural elements, respectively). Note that each mechanical mode and each electric mode (electrode pair) corresponds to a degree of freedom. Lastly, a generalized damping term, $\boldsymbol{C}\dot{\boldsymbol{r}}$ has been added to include all sources of mechanical damping, ζ_m.

When considering one beam mode (approximating the infinite degree-of-freedom mechanical system as a single-degree-of-freedom system) and a single electrode pair,[‡] the governing equations reduce to scalar equations. This allows for an extracted power optimization to be performed in closed form. Because one vibration mode is considered, the system will have a single natural frequency. For a structure with an active/piezoelectric component, the natural frequency depends on the electrical loading (electrical boundary condition); in the case of the extreme electrical loadings of short and open circuits, the natural frequency corresponds to the resonance and antiresonance frequency, respectively. In the scalar sensing equation, the charge can be related to the voltage through $v = R_l \frac{dq}{dt}$ (assuming a purely resistive electrical load which is small relative to the piezoelectric element leakage resistance) to obtain the scalar governing equations. Because the structure will generally have more than one electrode pair (corresponding to multiple active elements for the configuration considered here), the equations can also be written in terms of effective electric parameters (as determined in Sec. II.B):

$$M\ddot{r} + C\dot{r} + Kr - \theta v = -B_f \ddot{w}_B \qquad (8)$$

$$\theta \dot{r} + C_p \dot{v} + \frac{1}{R_l} v = 0 \qquad (9)$$

From these governing equations, the voltage developed and power extracted can be calculated. The magnitudes (or half peak-to-peak amplitude) of the voltage and power are frequently reported in the literature [3,14,15] and this paper will follow that convention. A closed form solution of the magnitudes for relative displacement, voltage developed and power extracted[§] can be obtained if harmonic base excitation (w_B) is assumed. The magnitude of the power is calculated through $|P_{out}| = |v|^2/R_l$:

$$\left| \frac{r}{B_f \ddot{w}_B} \right|$$
$$= \frac{1}{K} \frac{\sqrt{1 + (\alpha\Omega)^2}}{\sqrt{[(1 - \Omega^2) - 2\zeta_m \alpha\Omega^2]^2 + [(\{1 + \kappa^2\} - \Omega^2)\alpha\Omega + 2\zeta_m\Omega]^2}} \qquad (10)$$

$$\left| \frac{v}{B_f \ddot{w}_B} \right|$$
$$= \frac{1}{|\theta|} \frac{\alpha\kappa^2\Omega}{\sqrt{[(1 - \Omega^2) - 2\zeta_m \alpha\Omega^2]^2 + [(\{1 + \kappa^2\} - \Omega^2)\alpha\Omega + 2\zeta_m\Omega]^2}} \qquad (11)$$

$$\left| \frac{P_{out}}{(B_f \ddot{w}_B)^2} \right|$$
$$= \frac{\omega_1}{K} \frac{\alpha\kappa^2\Omega^2}{[(1 - \Omega^2) - 2\zeta_m \alpha\Omega^2]^2 + [(\{1 + \kappa^2\} - \Omega^2)\alpha\Omega + 2\zeta_m\Omega]^2} \qquad (12)$$

$\omega_1 = \sqrt{(K/M)}$ is the resonance frequency corresponding to the first mechanical mode of the structure (i.e., ω_r) and $\Omega = \frac{\omega}{\omega_1}$ is the frequency ratio. $\kappa^2 = \theta^2/KC_p$ is the system coupling term and $\alpha = \omega_1 R_l C_p$ is the dimensionless time constant. The generalized mechanical displacement should be multiplied by the mode shape (which is normalized to a factor 2 at the tip) to convert it to the relative displacement [9]. The next step is to optimize the power extracted,

which is detailed in duToit et al. [7]. The system can be analyzed at short- and open-circuit conditions by letting the electrical load resistance tend to zero and infinity, respectively. Two optimal frequency ratios for maximum power generation are obtained, which correspond to the resonance (subscript r) and antiresonance (subscript ar) frequencies of the beam structure:

$$\Omega_r = 1 \quad \text{and} \quad \Omega_{ar} = \sqrt{1 + \kappa^2} \qquad (13)$$

The antiresonance frequency (ω_{ar}) is determined by the coupling term. These resonant frequencies are clearly evident in the denominators of Eqs. (10–12). Moreover, it should be noted that when mechanical damping $\zeta_m \to 0$, the responses at resonances do not approach infinity because of the electrical damping (resistor) in the system, except for the short-circuit case ($R_l = 0 \Rightarrow \alpha = 0$) and the open-circuit case ($R_l = \infty \Rightarrow \alpha = \infty$). This is because no power is dissipated through the resistor for these special cases. The power can further be optimized with respect to load resistance to obtain an optimal electrical load. This is achieved by optimizing the power with respect to the dimensionless time constant α to obtain

$$\alpha_{opt}^2 = \frac{1}{\Omega^2} \frac{(1 - \Omega^2)^2 + (2\zeta_m\Omega)^2}{([1 + \kappa^2] - \Omega^2)^2 + (2\zeta_m\Omega)^2} \qquad (14)$$

where $\zeta_m = C/2M\omega_1$ is the damping ratio and is taken as constant in the vicinity of ω_r and ω_{ar}. Noting that $2\zeta_m/\kappa^2 \ll 1$ for many systems/devices, the power-optimal time constant α (or equivalent electrical load) at the resonance and antiresonance frequencies, Ω_r and Ω_{ar}, can be obtained from Eq. (14) as

$$\alpha_{opt,r} \approx \frac{2\zeta_m}{\kappa^2} \qquad (15)$$

$$\alpha_{opt,ar} \approx \frac{\kappa^2}{2\zeta_m(1 + \kappa^2)} \qquad (16)$$

Considering α_{opt} in Eqs. (15) and (16), it can be seen (again noting that $2\zeta_m/\kappa^2 \ll 1$) that the optimal resistance for power extraction at resonance is much less than at antiresonance ($R_{lopt,r} \ll R_{lopt,ar}$). Substituting the time constants obtained in Eqs. (15) and (16) into the power Eq. (12) (with $2\zeta_m/\kappa^2 \ll 1$), the following approximation is obtained for the maximum power at both the resonant and antiresonant operating points:

$$|P_{out}|_{opt,r} \approx |P_{out}|_{opt,ar} \approx \frac{B_f^2}{\sqrt{KM}} \frac{\ddot{w}_B^2}{8\zeta_m} \qquad (17)$$

This result suggests that the power extracted under optimal conditions at the two optimal frequencies (resonance and antiresonance, respectively) are equal. Secondly, the piezoelectric system coupling term (κ^2) cancels out of the power equation under optimal conditions, for these cases where $2\zeta_m/\kappa^2 \ll 1$. In fact, the only material properties that affect the maximum absolute power developed here are the density and stiffness (short circuit for the active material). This is a counterintuitive result which suggests that the specific active material used (e.g., PZT-5A vs PZT-5H—refer to [7]) has little effect on maximum power developed (under optimal conditions). Thus, although power is in general a strong function of coupling [via κ^2 in Eq. (12)], the optimum extracted power is independent of the coupling, provided that $2\zeta_m \ll \kappa^2$, which is generally true. α (and thus electrical resistance), voltage and current, important variables secondary to power, are strongly dependent on the piezoelectric properties and operating point selection.

The expressions for displacement, voltage, and power given by Eqs. (10–12) reveal some interesting characteristics. The electrical damping ratio ζ_e can be obtained from the mechanical displacement Eq. (10) by setting the mechanical damping ζ_m equal to zero to give

$$\left| \frac{r}{B_f \ddot{w}_B} \right| = \frac{1}{K} \frac{\sqrt{1 + (\alpha\Omega)^2}}{\sqrt{[1 - \Omega^2]^2 + [(1 + \kappa^2) - \Omega^2]^2 \alpha^2\Omega^2}} \qquad (18)$$

[‡]In the bimorph, the two electrode pairs can be reduced to a single effective pair, as shown in Sec. II.B.

[§]The average power developed will be 64% of the magnitude of the power.

At the resonance, $\Omega = 1$, this would give an equivalent damping ratio of

$$\zeta_{e,r} = \frac{\kappa^2 \alpha}{2\sqrt{1+\alpha^2}} \qquad (19)$$

whereas at the antiresonance frequency, $\Omega = \sqrt{1+\kappa^2}$, one obtains

$$\zeta_{e,\text{ar}} = \frac{\kappa^2}{2\sqrt{1+\alpha^2(1+\kappa^2)}} \qquad (20)$$

and between the two frequencies at $\Omega = \Omega_{\text{mp}} = \sqrt{1+\kappa^2/2}$ one obtains $\zeta_{e,\text{mp}} \approx \kappa^2/4$. The midpoint (between the resonance and antiresonance frequency) is particularly interesting as this point provides the maximum power density (power per device operating volume). As a rough approximation, one may add the mechanical and electrical damping to obtain the total damping and resulting response, but more rigorously one should go through the basic Eqs. (10–12) and (14). It is of interest to note that for the previously mentioned cases where $2\zeta_m/\kappa^2 \ll 1$, the optimum time constants of Eqs. (15) and (16) will combine with the electrical damping ratios above to give the relations for maximum power:

$$\zeta_{e,r} \approx \zeta_m \quad \text{and} \quad \zeta_{e,\text{ar}} \approx \zeta_m\sqrt{1+\kappa^2} \qquad (21)$$

for $\Omega = 1$ and $\Omega = \sqrt{1+\kappa^2}$, respectively. Between these two frequencies at Ω_{mp}, one has

$$\zeta_{e,mp} \approx \frac{\kappa^2}{4} \quad \text{and} \quad \alpha_{\text{opt,mp}} \approx \frac{1}{\sqrt{1+\kappa^2/2}} \qquad (22)$$

The increased electrical damping at Ω_{mp} reflects the ability of the piezoelectric element to damp out the beam motions when tuned to an appropriate value of α (i.e., electrical resistance R_l). Note further
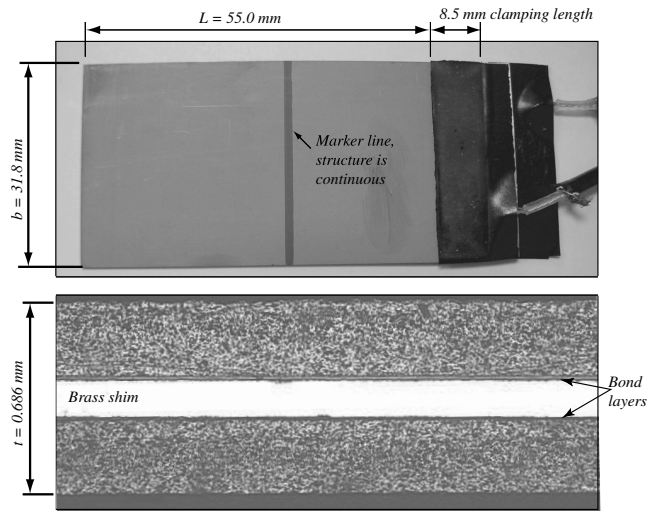

Fig. 1   Planform of device (top) and a cross section of the individual layers of the device (bottom).

that the power-optimal time constants (resistances) order themselves as follows (again taking $2\zeta_m/\kappa^2 \ll 1$): $\alpha_{\text{opt},r} \ll \alpha_{\text{opt,mp}} \ll \alpha_{\text{opt,ar}}$. The corresponding optimum power at Ω_{mp} becomes

$$|P_{\text{out}}|_{\text{opt,mp}} \approx \frac{B_f^2}{\sqrt{KM}} \frac{\ddot{w}_B^2}{\kappa^2/2[1+2(2\zeta_m/\kappa^2)\sqrt{1+\kappa^2/2}]^2} \qquad (23)$$

where the piezoelectric system coupling term, κ^2, is clearly important, in contrast to the trends at the resonances [see Eq. (17) and discussion thereafter].

B.   Test-Device Specific Model Implementation

The test device is a piezoelectric bender, which has a symmetric bimorph cantilevered structure with no proof mass at the tip (refer to Fig. 1). The device has two oppositely poled active elements and thus four electrodes (two pairs), which are illustrated in Fig. 2 (left). To account for the bimorph geometry while allowing the use of the optimization scheme, a reduction scheme is presented to compute the effective coefficients, $C_{p,e}$ and θ_e, for Eqs. (8) and (9). First, the effect of the piezoelectric element orientation needs to be discussed. The orientation of the piezoelectric element is defined by the poling of the element. Per convention, the material local coordinate x_3^l direction is always defined positive in the direction of poling. However, for analysis, all parameters must be analyzed in the global coordinates (x_3, x_2), which can be chosen arbitrarily. When the local coordinates of the element and the global coordinates do not align, adjustment of the constitutive relations are necessary. It is assumed here that the piezoelectric element local x_3^l direction is either parallel or antiparallel to the global x_3 direction. In this case, the piezoelectric constants (e_{31} for the bimorph analyzed herein) simply switches sign when the element is poled in the $-x_3$ (global) direction.

For the series electrical connection (see Fig. 2, right), the two elements are oppositely poled, such that in bending opposite and equal strains above and below the neutral axis generate electric fields that are in the same direction. Referring to Fig. 2 (left), the bottom piezoelectric element (2), is poled in the $-x_3$ direction and thus the negative of the piezoelectric constant should be used to determine the coupling term θ_2. The next step is to determine the effective system coupling and capacitive parameters in terms of the individual piezoelectric element parameters θ and C_p. The device is connected to the electrical load by shorting the two center electrodes (e_2 and e_3), and connecting the top (e_1) and bottom electrodes (e_4) across the electrical load. The effective circuit is presented in Fig. 2 (right) where the piezoelectric elements are represented as simple capacitors. From this circuit, note that $v_1 + v_2 = v$ and $q_1 = q_2 = q$. Thus, the two sensing equations [from Eq. (2)] can be summed and rewritten as

$$(\theta_1 + \theta_2)r + (C_{p,1}v_1 + C_{p,2}v_2) = -2q \qquad (24)$$

Assuming that the bimorph is perfectly symmetric, $\theta_1 = \theta_2$ and $C_{p,1} = C_{p,2}$, as well as $v_1 = v_2$ and $q_1 = q_2$. Thus, the equations of motion [Eqs. (1) and (2)] can be written in terms of piezoelectric element 1 parameters (v_1, q_1, θ_1, and C_{p1}):

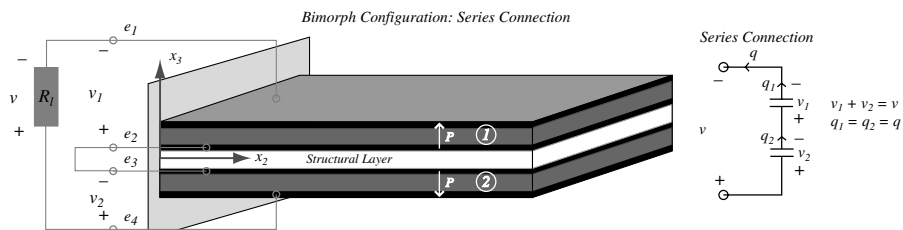$$M\ddot{r} + C\dot{r} + Kr - 2\theta_1 v_1 = -B_f\ddot{w}_B \qquad (25)$$

Fig. 2   Electrical connections: symmetric bimorph configuration (left) with oppositely poled active elements. The series connection (right) is illustrated with a simplified equivalent electrical circuit.

$$2\theta_1 r + 2C_{p,1}v_1 = -2q_1 \qquad (26)$$

Now, because the elements are connected in series, the charge (and current) through each element will be the same, $q = q_1$. The current is related to the charge through $i = \frac{dq}{dt}$ and the derivative of Eq. (26) with respect to time can be taken. The voltages developed across the individual elements will add ($v = v_1 + v_2 = 2v_1$) and the current is related to the voltage across the electrical load (assumed purely resistive) through $v = iR_l$, where R_l is the electrical load. Thus, the equations of motion become

$$M\ddot{r} + C\dot{r} + Kr - \theta_1 v = -B_f \ddot{w}_B \qquad (27)$$

$$\theta_1 \dot{r} + \frac{1}{2}C_{p,1}\dot{v} + \frac{1}{R_l}v = 0 \qquad (28)$$

By comparison to Eqs. (8) and (9), the effective coupling is equal to the coupling of the individual elements, $\theta_e = \theta_1$. The effective capacitive term is one-half the capacitance of the individual elements, $C_{p,e} = \frac{1}{2}C_{p,1}$, as expected for two identical capacitors connected in series. With these effective parameters, the equations of motion reduce to two scalar equations and the prior optimization scheme can be used to determine the performance of the system. The last step is to explicitly calculate the individual active element parameters.

Because the developed strains are opposite above and below the neutral axis, the electric fields developed in the active elements will be in the same direction. The corresponding electric potential varies from 0 at the top of each piezoelectric element, to $+1$ at the bottom of each element. This is captured through the form of the electrical mode shape, ψ_v:

$$\psi_v = \begin{cases} \frac{-x_3 + (\frac{t_s}{2} + t_p)}{t_p} & \text{for } x_3 > 0 \quad \text{(corresponding to element 1)} \\ \frac{-x_3 - \frac{t_s}{2}}{t_p} & \text{for } x_3 < 0 \quad \text{(corresponding to element 2)} \end{cases} \qquad (29)$$

The numbering of the active elements is indicated in Fig. 2 (left). The resulting electric fields are

$$E = -\nabla \psi_v = \begin{cases} \frac{1}{t_p} & \text{for } x_3 > 0 \\ \frac{1}{t_p} & \text{for } x_3 < 0 \end{cases} \qquad (30)$$

From Fig. 2 (left), it can be seen that the bottom element will have negative piezoelectric constant e_{31} as the poling direction is opposite the global x_3 direction. Conversely, the top element will have positive e_{31}. The coupling and capacitance terms were defined in Eqs. (5) and (6). Note that the mechanical mode shape accounts for the proof mass contribution (if present). Refer to [7] for the modal analysis accounting for an off-axis proof mass. Calculating these terms for the individual elements in the current geometry for each element, the following is obtained:

$$\theta_1 = \theta_2 = e_{31}^* \psi_r'(L) \left(\frac{t_p + t_s}{2} \right) b \qquad (31)$$

$$C_{p1} = C_{p2} = \frac{\varepsilon_{33}^{S*} b L}{t_p} \qquad (32)$$

$\psi_r'(L)$ is the spatial derivative of the mechanical mode shape evaluated at the beam tip (with no proof mass present). All the parameters necessary for the model implementation have now been obtained. Next the device dimensions and material properties are obtained and an experimental test matrix developed.

III.   Experimental Procedures

The experimental setup is described and a model-informed test matrix is established to measure the relevant material properties (such as the piezoelectric constant) and to investigate the electrical and mechanical performance of a macroscale piezoelectric vibration energy harvester (Piezo Systems, Inc. T226-A4-503X). The device was operated at a set of discrete base input frequencies and the electrical and mechanical response was measured for varying electrical loadings. The frequencies and electrical loads were selected to ensure both resonance and off-resonance device operation. These two operating regimes correspond to the large-strain and small-strain operations of the piezoelectric material, respectively. Voltage and transverse displacement data are documented (graphically and tabulated), in addition to the frequency and electrical loading at which the individual tests were performed.

A.   Experimental Setup

Two performance measures are of interest when concerned with model verification: the mechanical and the electrical performances. In the mechanical domain, the parameter of primary interest is the lateral tip displacement which is measured with a laser vibrometer (Polytec PSV-300H). Full mode shapes were captured with the laser vibrometer but are not reported herein. There are two electrical parameters from which the electrical performance of the device can be established: the output voltage and the power generated. The voltage output can be measured directly. The power generation is calculated from the output voltage and knowledge of the electrical loading. In this project, a purely resistive electrical load is used to simplify the calculation and measurement of the power. Last, the resonant and antiresonant frequencies are of interest as these couple both the mechanical and electrical domains. The experimental setup is illustrated in Fig. 3.

B.   Test-Device Dimensions and Material Properties

To minimize uncertainty in the modeling, the geometric parameters of the device, as well as material properties, were measured whenever possible. These parameters (summarized in Table 1) were used in the model implementation. The test device consists of two metallized (electroded) piezoelectric elements (PZT-5A), separated by a brass shim. The piezoelectric elements are oppositely poled, allowing for a series connection. The brass shim serves as the electrical connect between electrodes e_2 and e_3. The nickel electrode thicknesses are negligible [see Fig. 1 (bottom)].

The device was mounted on an electrostatic shaker with an aluminum clamp of length 8.5 mm, width ~45 mm, and thickness ~5 mm (see Fig. 4). A clamping pressure of 12.5 MPa, or 1800 Psi, was applied (the clamping area was 8.5 mm × 31.8 mm), which was controlled with a torque wrench. The length of the clamped device was $L = 55.0$ mm. The leads were connected to the electrical load resistance as illustrated in Fig. 2 (left).
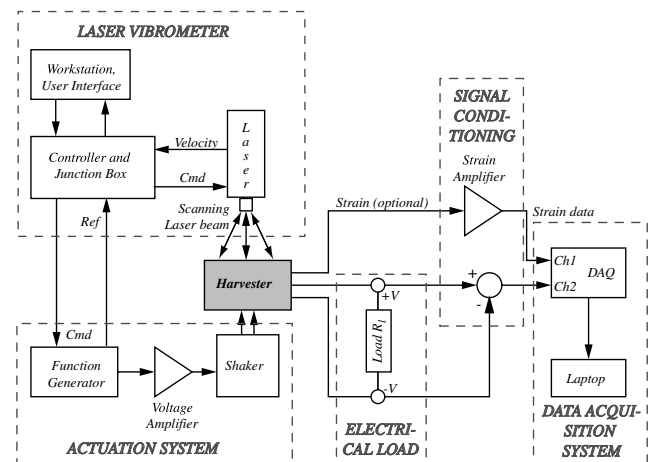

Fig. 3   Illustration of the experimental setup.

Table 1 Material properties for test device [PZT-5A bimorph from Piezo Systems, Inc. (T226-A4-503X)]

Material property	Used	Published	Ref.
Published properties used			
ρ_p, kg/m³	7800	7800	[16]
c_{11}^E, GPa[a]	66	66	[16]
d_{31}, m/V	-190×10^{-12}	-190×10^{-12}	[16]
Measured properties			
Device length (as acquired), L, mm	63.5	63.5	[16]
Device length (clamped, as tested), L, mm	55.0	——	——
Device width, b, mm	31.8	31.8	[16]
Piezolayer thickness, t_p, μm[b]	270	270	[16]
Structure layer thickness, t_s, μm[b]	140	130	[16]
Device mass, g	10.564	——	——
Capacitance (constant stress), C_p^T, nF	52.8	59.1	——
e_{31}, C/m²[a]	-14	——	——
Calculated properties			
ρ_s, kg/m³	7165	9000	[9]
ε_{33}^T, F/m	$1800 \times \varepsilon_0$	$1800 \times \varepsilon_0$	[16]
Elastic stiffness, structural layer, c_s, GPa	100	105	[9]
ε_{33}^S, F/m[a]	$1500 \times \varepsilon_0$	——	——

[a]Beam effective parameters; refer to duToit [9], p. 89.
[b]From microscopy measurements with Zeiss microscope.

All practical systems have damping. The damping affects the system response, especially near the resonances. Direct measurement of the mechanical damping ratio (ζ_m captures all nonelectrical damping) is necessary. This measurement must account for the damping terms associated with the drag-force, structural, and support damping terms [7]. Thus, a measurement scheme was developed for the damping during a dynamic test by comparing the base and absolute tip displacements. At the resonance frequency, and for short-circuit conditions (zero electrical load), absolute tip displacement, w_{tip}, is related to the base displacement through (assuming small damping)

$$\left| \frac{w_{tip}}{w_B} \right| \approx \frac{B_f}{M} \frac{1}{\zeta_m} \qquad (33)$$

The ratio of B_f and M is simply dependent on the mode shape, ψ_r, and is 0.783 for the current configuration (a cantilevered structure without a proof mass). Thus, the mechanical damping is conveniently related to the base and absolute tip displacements
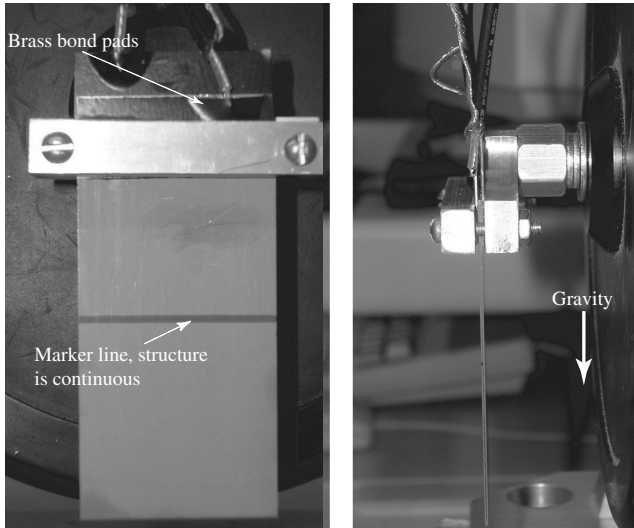

Fig. 4 The clamped device mounted on the electrostatic shaker: front view, or laser scan view (left), and side view (right). The indicated marker line appears on the as-acquired device and is of no structural consequence.

through $\zeta_m \approx 0.7830 |w_B/w_{tip}|$. Using this result, a mechanical damping ratio of $\zeta_m = 0.0178$ is calculated from measured base and tip displacements during a resonance (short-circuit) device operation when the structure is excited at 2.5 m/s².

Next, the material properties for the device are discussed. A detailed description of the methods used for these tests are give by duToit [9]. The material properties of interest are the elastic stiffness (both for the structure and the piezoelectric elements), the piezoelectric constant, and the permittivity. The average elastic stiffness of the device can be computed from knowledge of the device geometry and the resonance frequency (i.e., at short circuit). Material properties for the individual layers cannot be measured with ease for the device geometry under consideration. Thus, some assumptions are necessary to infer all the material properties. The published elastic stiffness ($c_{11}^{E*} = 66$ GPa) and density ($\rho_p = 7800$ kg/m³) for the piezoelectric elements are used. Using these properties, the density of the structural layer was calculated as $\rho_s = 7165$ kg/m³ and the elastic stiffness of the structural layer (brass) is 100 GPa. The piezoelectric coupling is calculated from the relative positions of the resonance and antiresonance frequencies. A piezoelectric constant of $e_{31}^* = -14$ C/m² is obtained, which compares well with the expected coupling of between -12 and -17.5 C/m² for a beam and plate, respectively (refer to [9], p. 89). Permittivity is inferred through capacitance measurements made with an impedance analyzer. The published bulk value of $\varepsilon_{33}^T = 1800\varepsilon_0$ F/m is confirmed through these tests. The permittivity at constant strain is calculated from the published value, using the determined piezoelectric constant, e_{31}^* and the bulk value of the piezoelectric constant relating strain to electric field, $d_{31} = -190 \times 10^{-12}$ m/V. The value obtained was $\varepsilon_{33}^{S*} = \varepsilon_{33}^T - d_{31}^2 c_{11}^E = 1500\varepsilon_0$ F/m. These results are summarized in Table 1, and are compared to published results where available. Using these properties for the device, the system coupling term $\kappa^2 = 0.118$. Further, the key device parameters in Eqs. (8) and (9) are $M = 9.12 \times 10^{-3}$ kg, $C = 0.218$ N·s/m, $K = 4.10 \times 10^3$ N/m, $\theta_e = -4.57 \times 10^{-3}$ N/V, $B_f = 7.14 \times 10^{-3}$ kg, and $C_{p,e} = 4.30 \times 10^{-8}$ F.

C. Modeling- and Optimization-Informed Performance Tests

From the model development and analysis presented by duToit et al. [7,9,11], a test matrix was developed to investigate key aspects of the predicted device response. Two prospective operating points were identified for piezoelectric energy harvesters. For low damping and high piezoelectric coupling, these operating points are approximately the resonance and antiresonance frequencies, respectively. The model predicts that the power extracted at these operating points should be equal. Thus, to verify the model, experimental data are required for operation at both the resonance and antiresonance frequencies, as well as away from these frequencies. To accomplish this goal, two tests were performed: first, the resonance and antiresonance frequencies are determined by exciting the system at a spectrum of frequencies and measuring the mechanical response (via a tip-displacement measurement with a laser vibrometer). To obtain the resonance frequency, the short-circuit electrical condition is enforced. For the antiresonance frequency measurement, an open-circuit condition is applied. Second, the device is driven at a constant base input acceleration (2.5 m/s²) at various frequencies and under varying electrical loads. The electrical response (via resistance and voltage measurements to calculate power) and mechanical response are obtained. This test is used to investigate the two device operating regimes: *resonant operation* (driven at either resonance or antiresonance frequency) and *off-resonant operation*.

IV. Model Verification

In this section, the measurement data for the test device are presented and compared with the modeling results. First, the positions of the resonance and antiresonance frequencies are compared, as are the optimal electrical loadings (the electrical
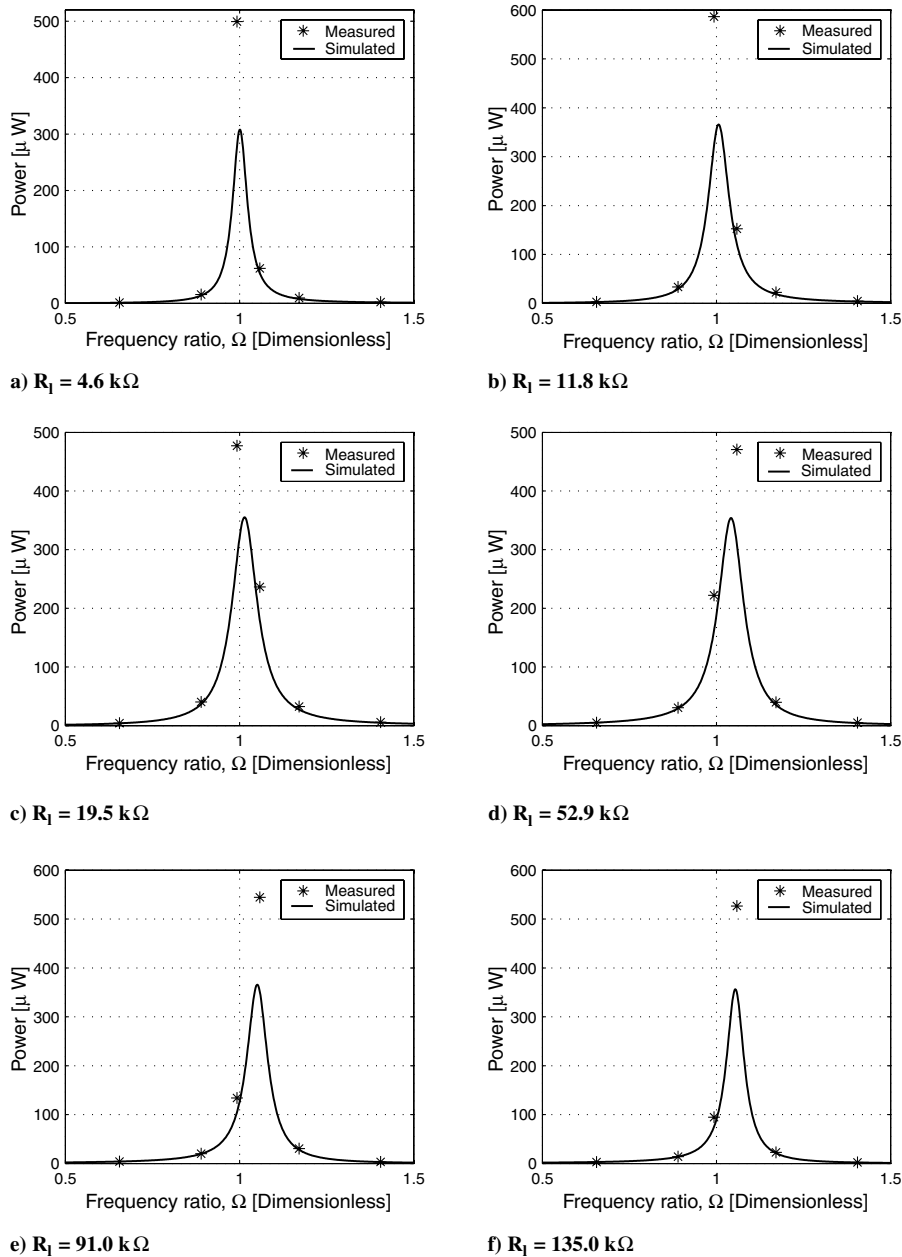
a) $R_l = 4.6 \text{ k}\Omega$

b) $R_l = 11.8 \text{ k}\Omega$

c) $R_l = 19.5 \text{ k}\Omega$

d) $R_l = 52.9 \text{ k}\Omega$

e) $R_l = 91.0 \text{ k}\Omega$

f) $R_l = 135.0 \text{ k}\Omega$

Fig. 5 Predicted vs measured power plotted vs frequency for varying electrical loads. Base acceleration is held constant at 2.5 m/s^2. $f_r = 107$ Hz, and $f_{ar} = 113$ Hz.

loading required for maximum power generation at resonance and antiresonance, respectively). Next, the overall response of the system is investigated. Consistent with the preliminary model validation [7] to work in the open literature, the correlation of the model to experimental results depends on the operating regime (i.e., at or away from resonance). The off-resonant and resonant operation results (experimental and simulated) for the system are compared. It is found that the model consistently underpredicts the electrical performance of the device during resonance operation. This phenomenon is investigated experimentally and the model deviation is explained by observed nonlinear piezoelectric coupling at larger strain. Tabulated experimental data are provided in the Appendix to supplement the figures.

A. Resonance Frequency, Antiresonance Frequency, and Optimal Resistances

The first comparison between the simulation and the measurements is in the position of the resonance and antiresonance frequencies. The measured results show the resonance and antiresonance frequencies of $f_r = 106.5$ to 107.8 Hz and $f_{ar} = 112$ to 113.8 Hz, respectively. This is compared to the predictions of $f_r = 106.8$ Hz and $f_{ar} = 112.9$ Hz. Given that published material properties were used for the piezoelectric material elastic stiffness, the results for the resonance frequency agree very well. The antiresonance frequency is a function of the elastic stiffness of the device and the piezoelectric coupling. This experimental value was used to calculate the piezoelectric constant e_{31}^*.

The optimal electrical loading for maximum power extraction was determined by exciting the device at either the resonance or antiresonance frequencies and sweeping through electrical loads by using discrete resistors (resistance measured using standard multimeter). The base acceleration (2.5 m/s^2) was held constant during these tests by monitoring the base acceleration with the laser vibrometer. The measured values for maximum power were $R_{l,r} = 11$ kΩ and $R_{l,ar} = 100$ kΩ. These again compare very well with the predicted values of $R_{l,r} = 10.0$ kΩ and $R_{l,ar} = 108$ kΩ. These results suggests that the model captures the overall response of the structure at and around the resonances. The next step is to compare the predicted and measured response (including voltage and power).

a) Frequency = 70 Hz

b) Frequency = 95 Hz

c) Resonance = 107 Hz

d) Antiresonance = 113 Hz

e) Frequency = 125 Hz
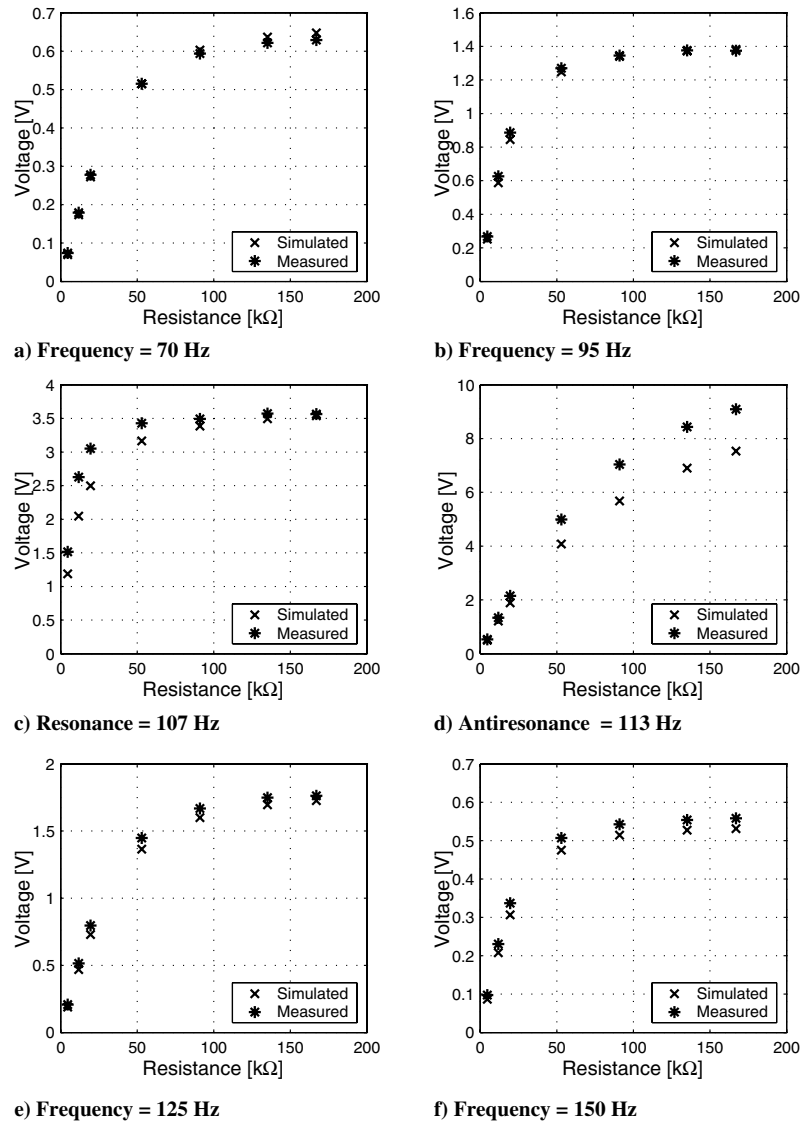
f) Frequency = 150 Hz

Fig. 6 Predicted vs measured response: voltage plotted against the electrical load at various input frequencies, corresponding to both off-resonance and resonance/antiresonance frequencies. Base acceleration was held constant at 2.5 m/s^2.

B. Overall Device Response

First, the overall response of the system is presented. The power is plotted vs varying frequency ratio for different electrical loads in Fig. 5. It is clear that there are indeed two design points, corresponding to the resonance frequency and the antiresonance frequency where the power is very nearly equal. The predicted results are in excellent agreement during off-resonant operation (in the small-strain regime), but there is significant deviation from the experimental results during resonant operation. The model underpredicts the electrical response of the system during resonant operation. The resonant and off-resonant operating regimes are discussed in detail in the sections to follow.

C. Off-Resonant Operation

The electrical and mechanical response of the system during off-resonant operation is now presented. The tabulated results are included in the Appendix for the voltage generated, the power generated, and the relative tip displacements. The voltage data are presented in Fig. 6 where it can be seen that the model predicts the device electrical response very well when operated away from the resonance frequencies (refer to Figs. 6a, 6b, 6e, and 6f). In Figs. 6a and 6f, the device is operated well away from the resonances and the model and experimental data agree. In Fig. 6c, the driving frequency was the resonance frequency. At low electrical loads, the deviation

between the measured and predicted response is pronounced. However, at higher electrical loads, the electrical loading approaches the open-circuit condition and the natural frequency of the device shifts to the antiresonance frequency. Thus, the device is effectively operated away from the resonances, and the simulations and measured results align well. The converse is also true at antiresonance, as seen in Fig. 6d. At low electrical loads, the natural frequency corresponds to the resonance frequency, and the device is effectively operated away from resonance. The simulated and predicted results align well there. However, at higher electrical loads, the device natural frequency coincides with the antiresonance frequency, and the model consistently underpredicts the electrical response. Similar trends are observable for Figs. 6b and 6e.

When comparing the power developed, as shown in Fig. 7, the same trends in model agreement are observable. The power is calculated from the square of the voltage and resistance measurements and any errors in these measurements will accumulate (especially errors in the voltage measurements). It is observed that the maximum power developed at the resonance frequency (~590 μW) is slightly higher than at the antiresonance frequency (~550 μW), in contrast with the equal power predicted by the model. This disagreement is addressed in Sec. IV.E. In Fig. 7, the sharp increase in resistance required for maximum power between resonant and antiresonant operation [as discussed with Eqs. (15) and (16)] should be noted.
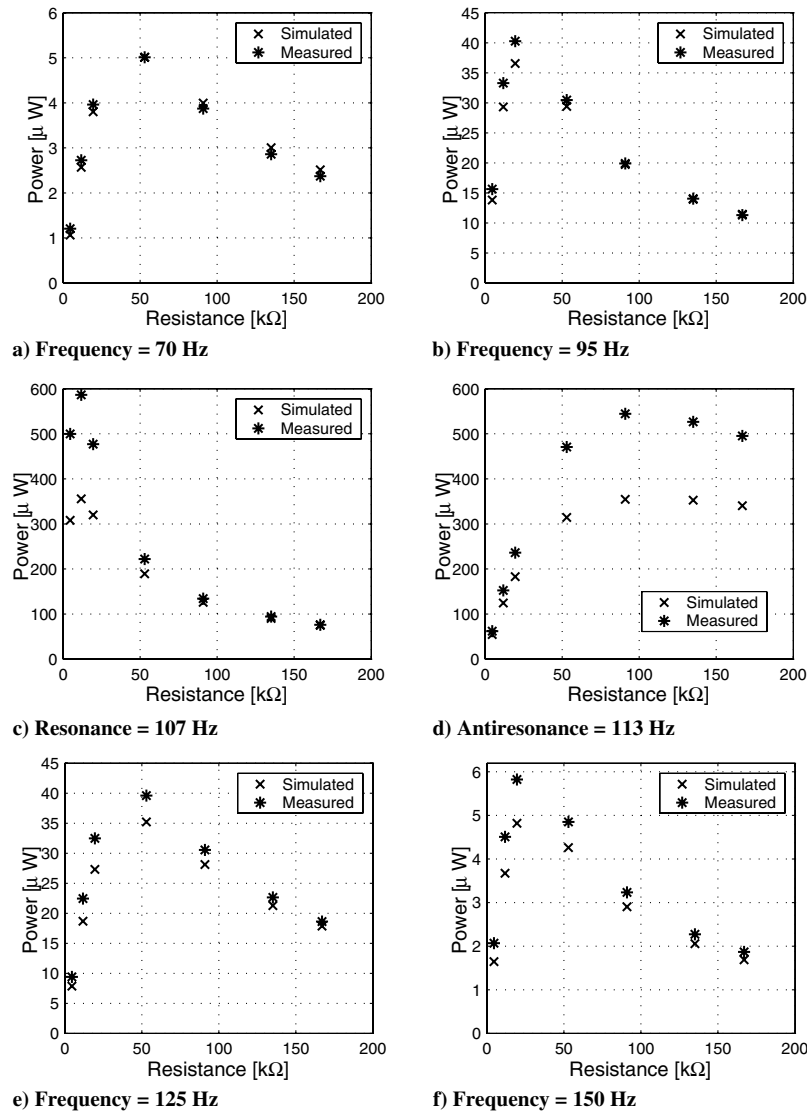
Fig. 7 Predicted vs measured response: power plotted against electrical load at various input frequencies, corresponding to both off-resonance and resonance/antiresonance frequencies. Base acceleration was held constant at 2.5 m/s².

Last, the predicted and measured mechanical response of the system is compared using the tip displacement in Fig. 8. Again, the same trends as above are observed: good correlation away from the resonances, underprediction around the resonances. It would be expected that the predicted relative tip displacement at resonance frequency should agree with the measured tip displacement at the low electrical load since, at low electrical loads, the short-circuit electrical condition is approached. This is not observed because the lowest electrical load at which a measurement was taken was 4.61 kΩ, which is a finite and not zero (short-circuit) condition. The mechanical damping was measured at zero electrical load (no piezoelectric coupling) and tip displacement aligns perfectly for this condition because the damping was determined using the measured tip and base displacement ratio.

D. Resonant Operation

From the previous section it is clear that the simulated response differed from the measured response at or near the resonances. This phenomenon was investigated in more detail, as summarized in Table 2. The device was driven at the resonance and antiresonance frequencies, respectively, while varying the electrical load. The driving signal magnitude was adjusted for each measurement to ensure that the base input acceleration was kept constant ($\ddot{w}_B = 2.5$ m/s²) as before. Note that the power densities calculated

are based on both the device volume (stationary) and the operating volume.

The electrical load was varied from $4.6 \rightarrow 167$ kΩ. The simulated and measured electrical responses are shown in Fig. 9. It is clear that the model predicts the trends and locations of the power maxima correctly, but the measured voltages are consistently high as compared to the simulation. Because the power is a function of the voltage squared, the errors in the power predictions are more substantial. It is interesting to note that again the simulation and measurements are in good agreement away from resonance (at high electrical loading the natural frequency of the device corresponds to the antiresonance frequency).

The simulated and measured results were also compared at the antiresonance frequency. As with the resonance frequency operation, the model consistently underpredicts the performance of the device. However, away from the antiresonance frequency (for low electrical loading), the correlation between the modeled and measured performance is again excellent. The measured maximum power at the antiresonance frequency was slightly lower than at resonance. This was contrary to predictions that showed equal maximum power at the resonance and antiresonance frequencies should be obtained. Overall, the model predicts the response of the device at resonances well (e.g., the optimal electrical loadings and trends), except that the magnitudes of predictions are consistently low for power and voltage.

Table 2 Predicted vs experimental result for test device during resonant operation

Parameter	Resonance frequency		Antiresonance frequency	
	Measured	Predicted	Measured	Predicted
Tip displacement, μm	151	120	140	114
Footprint area, cm^2	17.5	17.5	17.5	17.5
Device volume, cm^3	1.19	1.19	1.19	1.19
Operating volume, cm^3	1.72	1.61	1.68	1.59
Voltage, V	2.63	2.05	7.04	5.68
Power, μW	586	356	545	354
Power density, μW/cm^{2a}	33.5	20.3	31.1	20.3
Power density, μW/cm^{3b}	493	299	460	298
Power density, μW/cm^{3c}	341	221	324	223

[a]Calculated from the footprint area of a single device.
[b]Calculated from the volume of a single device.
[c]Calculated from the operating volume of a single device.

E. Unmodeled Piezoelectric Response

From the above discussion it is clear that the model predicts the response of the device at off-resonant operation very well, but generally underpredicts the electrical and mechanical response at the resonances. This has been ascribed to the linear small-signal model used to model the piezoelectric effect (in the constitutive relations).
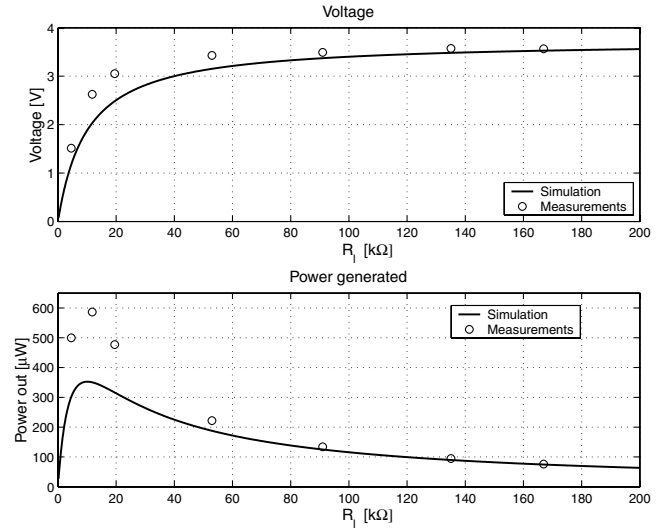
Fig. 9 Predicted vs measured response at the resonance frequency (107 Hz): voltage (top) and power (bottom) plotted vs electrical load for constant base acceleration. Note that at high R_l, the device natural frequency is at the antiresonance frequency and thus the natural frequency is not excited.
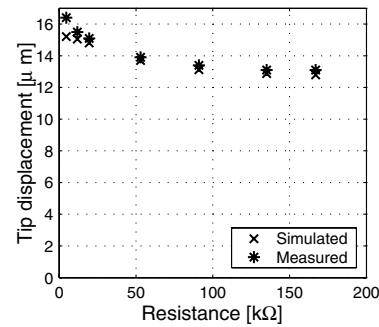
a) Frequency = 70 Hz
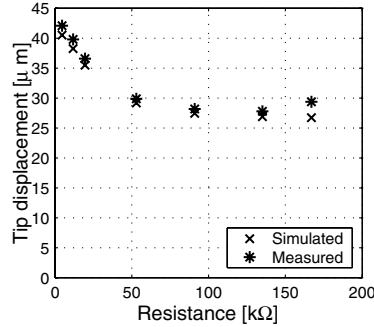
b) Frequency = 95 Hz
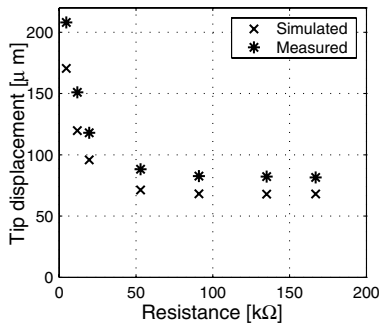
c) Resonance = 107 Hz
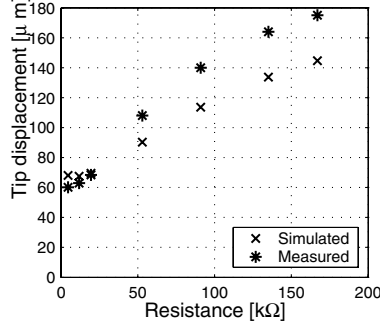
d) Antiresonance = 113 Hz
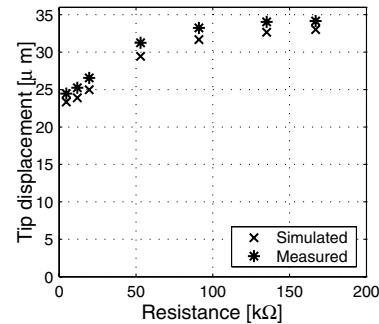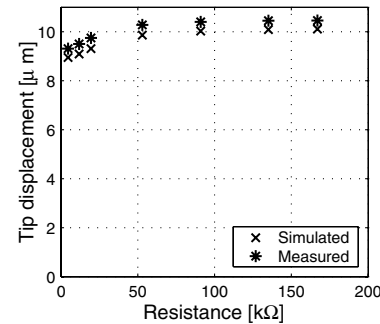
e) Frequency = 125 Hz

f) Frequency = 150 Hz

Fig. 8 Predicted vs measured response. Relative tip displacement plotted against electrical load at various input frequencies, corresponding to both off-resonance and resonance/antiresonance frequencies. Base acceleration was held constant at 2.5 m/s^2.
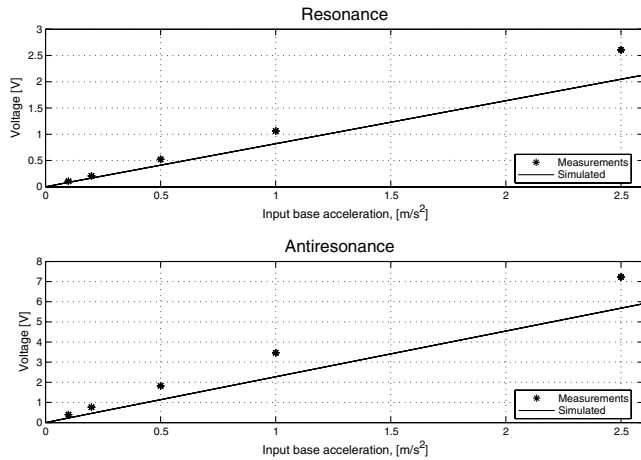
Fig. 10 Voltage developed at resonance (top) and antiresonance (bottom) frequencies for varying base input accelerations. Simulated values use the small-strain (linear) piezoelectric coupling coefficient.

As an example, Crawley and Anderson [17] experimentally documented the deviation of the piezoelectric constant, d (which is inversely proportional to e), from the linearized model at varying mechanical loadings (applied strain). It was shown that the piezoelectric coupling d deviates by as much as a factor of 70% *increase* at $100 \, \mu$ strain from the small-strain response. From the optimization analysis, one can show that under optimal conditions, the voltages developed at the resonance and antiresonance frequencies, respectively, are proportional to the piezoelectric

coupling constant. This result can be obtained by evaluating Eq. (14) at Ω_r and Ω_{ar} (assuming $\zeta_m \ll 1$) and substituting into Eq. (11):

$$|v|_{\text{opt},r} = \frac{1}{2|\theta|} B_f \ddot{w}_B \quad \text{and} \quad |v|_{\text{opt,ar}} = \frac{\alpha_{\text{opt,ar}}}{2|\theta|} B_f \ddot{w}_B \qquad (34)$$

θ is proportional to e according to Eq. (5). During resonant operation, the mechanical response (tip displacement) of the device is much larger than off-resonant operation, and the developed strains in the piezoelectric elements are higher. At the base of the structure and on the outer surfaces (farthest point from the neutral axis), a maximum strain of $\sim 5 \, \mu$ strain at $R_l = 4.61$ kΩ and 70 Hz, compared to $\sim 50 \, \mu$ strain at $R_l = 11.8$ kΩ and at the resonance frequency at the same location. To investigate the nonlinear effect of strain on the piezoelectric coupling coefficient qualitatively, the device was excited at resonance and antiresonance frequency and the input base acceleration was varied. During the resonance frequency test, the electrical loading was kept constant at $R_l = 11.93$ kΩ and at $R_l = 100.2$ kΩ for the antiresonance test. The results are given in Fig. 10. The small-signal piezoelectric constitutive law accurately predicts the electrical response for small mechanical loading (corresponding to a small base acceleration and small strain), but at larger loadings/strains the electrical response deviates significantly from the expected value. For a given input acceleration, the voltage developed is higher than expected, indicating an increase in piezoelectric coupling. One might expect better results when a more appropriate value for the piezoelectric coupling is used, but it should be noted that the constant was obtained from the relative positions of the resonance and antiresonance frequencies, which were measured at small base excitation levels (on the order of 0.04 m/s^2) and

Table A1   Experimental results for 70, 95, 107, 113, 125, and 150 Hz tests for varying electrical loads

Resistance, kΩ	4.61	11.91	55.90	100.1	156.2	200.4
Frequency = 70 Hz, $\ddot{w}_B = 2.5$ m/s^2						
Voltage, V	0.074	0.179	0.515	0.594	0.621	0.629
Power, μW	1.20	2.73	5.01	3.87	2.86	2.37
Absolute tip displacement, μm	29.3	28.4	26.8	26.3	26.0	26.0
Base displacement,[a] μm	−12.9	−12.9	−12.9	−12.9	−12.9	−12.9
Relative tip displacement, μm	16.4	15.5	13.9	13.4	13.1	13.1
Frequency = 95 Hz, $\ddot{w}_B = 2.5$ m/s^2						
Voltage, V	0.268	0.626	1.270	1.346	1.377	1.374
Power, μW	15.62	33.28	30.47	19.90	14.03	11.31
Absolute tip displacement, μm	49.1	46.8	36.9	35.2	34.8	36.4
Base displacement,[a] μm	−7.02	−7.02	−7.02	−7.02	−7.02	−7.02
Relative tip displacement, μm	42.1	39.8	29.9	28.2	27.8	29.4
Resonance frequency = 107 Hz, $\ddot{w}_B = 2.5$ m/s^2						
Voltage, V	1.514	2.627	3.428	3.492	3.572	3.565
Power, μW	499.5	586.3	222.0	134.0	94.46	76.13
Absolute tip displacement, μm	208.0	151.0	82.6	77.0	76.6	75.9
Base displacement,[a] μm	0.00	0.00	5.64	5.64	5.64	5.64
Relative tip displacement, μm	208.0	151.0	88.2	82.6	82.2	81.5
Antiresonance frequency = 113 Hz, $\ddot{w}_B = 2.5$ m/s^2						
Voltage, V	0.533	1.339	4.992	7.039	8.435	9.093
Power, μW	61.86	152.3	470.7	544.5	526.6	495.2
Absolute tip displacement, μm	65.1	67.9	108.0	140.0	164.0	175.0
Base displacement,[a] μm	−4.96	−4.96	0.00	0.00	0.00	0.00
Relative tip displacement, μm	60.1	62.9	108.0	140.0	164.0	175.0
Frequency = 125 Hz, $\ddot{w}_B = 2.5$ m/s^2						
Voltage, V	0.208	0.514	1.448	1.667	1.749	1.762
Power, μW	9.40	22.45	39.58	30.55	22.64	18.61
Absolute tip displacement, μm	20.4	21.2	27.2	29.2	30.0	30.1
Base displacement,[a] μm	4.05	4.05	4.05	4.05	4.05	4.05
Relative tip displacement, μm	24.5	25.3	31.3	33.3	34.1	34.2
Frequency = 150 Hz, $\ddot{w}_B = 2.5$ m/s^2						
Voltage, V	0.097	0.230	0.507	0.542	0.554	0.558
Power, μW	2.07	4.51	4.85	3.23	2.27	1.87
Absolute tip displacement, μm	6.50	6.69	7.47	7.59	7.64	7.65
Base displacement,[a] μm	2.81	2.81	2.81	2.81	2.81	2.81
Relative tip displacement, μm	9.31	9.50	10.3	10.4	10.5	10.5

[a]For low damping, the absolute tip and base displacements are approximately in phase below the resonant frequency, approximately out of phase above the resonant frequency, and have an approximate phase shift of 90 deg near the resonance frequency (where the relative displacement is large compared to the base displacement) [9].

therefore small strains. Thus, the small-signal linear piezoelectric constitutive model is not sufficient to describe the device response during resonant operation.

The contribution of piezoelectric nonlinearity in the large-strain regime at the base input acceleration of 2.5 m/s^2 used in our tests quantitatively supports the strain nonlinearity as the source of voltage and power underprediction at the resonances. The voltage and power underprediction (0.5 V and 200 μW) at resonance ($R_l = 11.93$ kΩ) in Fig. 9 correspond to the difference measured in Fig. 10 (top, for resonance) at 2.5 m/s^2:0.5 V, which corresponds to a 150% increase in power (200 μW).

Second, the nonlinearity also explains the observed lower maximum power developed at antiresonance (as compared to resonance); the model predicts these values should be equal [see Eq. (17) and discussion] using the linear small-strain law. At resonance, the maximum strain developed in the device is 10% higher than at the antiresonance frequency. Thus, a higher piezoelectric constant can be expected (due to the nonlinear relationship between applied strain and this constant). The voltage is proportional to the piezoelectric constant, and the power is proportional to the voltage squared. Thus, this difference in strain can easily translate into the 3% decline in piezoelectric constant required to result in a 10% variation in the power developed.

Thus, piezoelectric large-signal vs small-signal constitutive response adequately explains the model underprediction at the resonances. Structural nonlinearity is not an explanation, given the magnitude of the tip displacements at the resonances.

V.   Conclusions

Experimental results for a piezoelectric vibration energy harvester are obtained and presented here, focusing on resonant vibrating, cantilevered devices that can be implemented in MEMS sensors. The experimental investigation is necessitated by the lack of comprehensive experimental results in the open literature, suitable for model verification that addresses the key operating points of resonance and antiresonance. A previously developed coupled electromechanical model is implemented for the experimental device. The obtained experimental results are used to verify the developed coupled electromechanical model and a useful design tool is obtained. The device response trends are captured through the model, though the electrical performance near the resonances is underpredicted. This is due to the nonlinear response of the piezoelectric material. The verified model has subsequently been applied to the design of a low-level, low-frequency MEMS-scale piezoelectric energy harvester [11] with the knowledge that the predicted optimal power will be very conservative due to the unmodeled nonlinear piezoelectric response. Future work on this research topic includes the fabrication and testing of an optimally designed microfabricated piezoelectric vibration energy harvester for aircraft SHM systems, as well as the investigation of alternative, compliant configurations for low-frequency vibration energy harvesters.

Appendix

Experimental results for the test device are presented in tabulated form in Table A1. The signs of the base displacements account for the correction necessary to calculate the relative displacements [9].

References

[1] Welsh, E., Fish, W., and Frantz, J. P., "Gnomes: A Testbed for Low Power Heterogeneous Wireless Sensor Networks," *Proceedings of the 2003 IEEE International Symposium on Circuits and Systems*, IEEE, Piscataway, NJ, 2003, Vol. 4, pp. 836–839.

[2] Rabaey, J. M., Ammer, M. J., da Silva, J. L. J., Patel, D., and Roundy, S., "PicoRadio Supports Ad Hoc Ultra-Low Power Wireless Networking," *Computer*, Vol. 33, No. 7, 2000, pp. 42–48.

[3] Roundy, S., Wright, P. K., and Rabaey, J. M., *Energy Scavenging for Wireless Sensor Networks with special focus on Vibrations*, Kluwer Academic Publishers, Norwell, MA, 2004.

[4] Amirtharajah, R., and Chandrakasan, A. P., "Self-Powered Signal Processing Using Vibration-Based Power Generation," *IEEE Journal of Solid-State Circuits*, Vol. 33, No. 5, 1998, pp. 687–695.

[5] Chandrakasan, A., Amirtharajah, R., Goodman, J., and Rabiner, W., "Trends in Low Power Digital Signal Processing," *IEEE International Symposium on Circuits and Systems, ISCAS*, IEEE, Piscataway, NJ, 1998, Vol. 4, pp. 604–607.

[6] Rabaey, J. M., Ammer, J., Karalar, T., Li, S., Otis, B., Sheets, M., and Tuan, T., "PicoRadios for Wireless Sensor Networks: The Next Challenge in Ultra-Low-Power Design," *2002 IEEE International Solid-State Circuits Conference*, IEEE, Piscataway, NJ, 2002, pp. 156–157.

[7] duToit, N. E., Wardle, B., and Kim, S., "Design Considerations for MEMS-Scale Piezoelectric Mechanical Vibration Energy Harvesters," *Journal of Integrated Ferroelectrics*, Vol. 71, 2005, pp. 121–160.

[8] Moheimani, S. R., "A Survey of Recent Innovations in Vibration Damping and Control Using Shunted Piezoelectric Transducers," *IEEE Transactions on Control Systems Technology*, Vol. 11, No. 4, 2003, pp. 482–494.

[9] duToit, N. E., "Modeling and Design of a MEMS Piezoelectric Energy Harvester," S.M. Thesis, Department of Aeronautics and Astronautics, Massachusetts Institute of Technology, 2005.

[10] Sodano, H. A., Park, G., and Inman, D. J., "Estimation of Electric Charge Output for Piezoelectric Energy Harvesting," *Strain*, Vol. 40, No. 2, 2004, pp. 49–58.

[11] duToit, N. E., and Wardle, B., "Performance of Microfabricated Piezoelectric Vibration Energy Harvesters," *Journal of Integrated Ferroelectrics*, Vol. 83, 2006, pp. 13–32.

[12] Mracek, A., "Towards an Embeddable Structural Health Monitoring Sensor: Design and Optimization of MEMS Piezoelectric Vibration Energy Harvesters, S.M. Thesis, Department of Aeronautics and Astronautics, Massachusetts Institute of Technology, 2006.

[13] Standard, M., "MIL-STF-810F, Annex C, Method 514.5," 1 Jan. 2000.

[14] Roundy, S., Wright, P. K., and Rabaey, J. M., "A Study of Low Level Vibrations as a Power Source for Wireless Sensor Nodes," *Computer Communications*, Vol. 26, No. 11, 2003, pp. 1131–1144.

[15] Sodano, H. A., Inman, D. J., and Park, G., "A Review of Power Harvesting from Vibration Using Piezoelectric Materials," *Shock and Vibration Digest*, Vol. 36, No. 3, 2004, pp. 197–205.

[16] Piezo Systems, Inc., 186 Massachusetts Avenue, Cambridge, MA 02139, Piezoelectric Engineering & Manufacturing Catalog No. 5, Jan. 2005.

[17] Crawley, E., and Anderson, E., "Detailed Models of Piezoceramic Actuation of Beams," *Journal of Intelligent Material Systems and Structures*, Vol. 1, No. 1, 1990, pp. 4–25.

M. Ahmadian
Associate Editor